ATLAS NOTE

ATLAS-CONF-2011-132

August 21, 2011

Search for neutral MSSM Higgs bosons decaying to $\tau^+\tau^-$ pairs in proton-proton collisions at $\sqrt{s} = 7$ TeV with the ATLAS detector

The ATLAS Collaboration

Abstract

A search for neutral Higgs bosons decaying to pairs of τ leptons with the ATLAS detector at the LHC is presented. Four different di-τ decay final states, $\tau\tau \rightarrow e\mu 4\nu$, $e\tau_{\mathrm{had}}3\nu$, $\mu\tau_{\mathrm{had}}3\nu$, and $\tau_{\mathrm{had}}\tau_{\mathrm{had}}2\nu$, where τ_{had} stands for τ leptons reconstructed in a hadronic final state, are considered. The analysis is using proton-proton collision events at a center-of-mass energy of 7 TeV, recorded in 2011 and corresponding to an integrated luminosity of 1.06 fb^{-1}. After signal selection, 4630 events are observed in this data sample. The observed number of events is consistent with the total expected background of 4900 ± 600 events. Exclusion limits at the 95% confidence level are derived for the production cross section of a generic Higgs boson ϕ as a function of the Higgs boson mass and for $A/H/h$ production in the Minimal Supersymmetric Standard Model (MSSM) as a function of the parameters m_A and $\tan\beta$ in the m_h^{max} scenario.

1 Introduction

Discovering the mechanism responsible for electroweak symmetry breaking and the origin of mass for elementary particles is one of the primary goals of the physics program at the Large Hadron Collider (LHC) [1]. In the Standard Model (SM), this mechanism requires the existence of a scalar particle, the Higgs boson [2–6]. For the minimal supersymmetric extension to the Standard Model (MSSM) [7,8], two Higgs doublets of opposite hypercharge are required, resulting in five observable Higgs bosons. Three of these Higgs bosons (the CP even h, H, and the CP odd A) are electrically neutral, while two are charged ($H^{\pm}$). At tree level and in the absence of CP-violating phases their properties such as masses, widths, and branching ratios can be predicted in terms of only two parameters, often chosen to be the mass of the CP-odd Higgs boson, m_A, and the ratio of the vacuum expectation values of the two Higgs doublets, $\tan\beta$.

In the MSSM, the strength of the effective Higgs boson couplings to fermions and gauge bosons is different from those in the Standard Model, resulting in different production cross sections and decay rates. While decays into ZZ or WW are dominant in the Standard Model for Higgs boson masses above ≈ 140 GeV, in the MSSM these decay modes are either suppressed by $\cos^2(\beta - \alpha)$, where α is the mixing angle of the two CP-even Higgs bosons, for the H boson or even absent for the A boson. However, the coupling of the Higgs boson to third-generation down-type fermions is strongly enhanced for large regions of the MSSM parameter space. Hence, the decay of the neutral Higgs bosons into a pair of τ leptons is one of the most promising channels for Higgs boson searches at the LHC. In the MSSM, Higgs boson production proceeds mainly via gluon fusion or in association with b quarks, where the latter is enhanced by $\tan^2\beta$ and thus becomes more important for large values of $\tan\beta$.

In this note, a search with the ATLAS detector [9] for neutral MSSM Higgs bosons in the decay mode $A/H/h \to \tau^+\tau^-$ is presented. The search considers Higgs boson decays to $e\mu 4\nu$, $e\tau_{had}3\nu$, $\mu\tau_{had}3\nu$, and $\tau_{had}\tau_{had}2\nu$, in the following referred to as $e\mu$, $e\tau_{had}$, $\mu\tau_{had}$ and $\tau_{had}\tau_{had}$. These decays have branching ratios of 6%($e\mu$), 23%($e\tau_{had}$), 23%($\mu\tau_{had}$), and 42%($\tau_{had}\tau_{had}$). The combination of $e\tau_{had}$ and $\mu\tau_{had}$ is referred to as $\ell\tau_{had}$. Similar searches for neutral Higgs bosons have been performed at the Tevatron [10, 11] and the LHC [12,13].

With respect to an earlier ATLAS search [13], this analysis is based on an about thirty times larger data set, uses an improved $\tau\tau$ mass reconstruction technique for the $\ell\tau_{had}$ final states and the $\tau_{had}\tau_{had}$ final state has been added.

2 Data and simulated samples

The data used in this search were recorded with the ATLAS detector in proton-proton collisions at a center-of-mass energy of $\sqrt{s} = 7$ TeV during the 2011 LHC run. The ATLAS detector is described in detail elsewhere [9]. In the ATLAS coordinate system, polar angles θ are measured with respect to the LHC beamline and azimuthal angles ϕ are measured in the plane transverse to the beamline. The pseudorapidity η is defined as $\eta = -\ln\tan\frac{\theta}{2}$. The transverse momentum is computed from the three-momentum p as $p_T = |p|\,\sin\theta$. The integrated luminosity of the data sample, considering only data-taking periods where all relevant detector subsystems were fully operational, is (1.06 ± 0.04) fb^{-1} [14].

The data were collected using a single-electron trigger with a p_{T} threshold of 20 GeV for the $e\mu$ and $e\tau_{had}$ final states; a single-muon trigger with a p_{T} threshold of 18 GeV was required for the $\mu\tau_{had}$ final state and as well as for the $e\mu$ final state if the event was not triggered by an electron. With respect to the event selection described in Section 4, the total trigger efficiencies are 99% and 82% for electrons and muons respectively. In the $\tau_{\mathrm{had}}\tau_{\mathrm{had}}$ channel events are selected by a dedicated hadronic τ decay trigger, which requests that at least two hadronic τ decays are reconstructed in the event. The ATLAS τ trigger is divided into three levels [9]. At the first level a transverse energy threshold based on coarse granularity calorimeter information is applied. This is then refined at the higher level triggers where the full granularity of the calorimeter data and noise suppression algorithms are available. Additionally, at the higher level triggers, shape variables are built and tracks of charged particles are reconstructed, in order to require narrow energy deposition and low charged track multiplicity, which are typical signatures of a τ_{had} decay. The transverse energy thresholds applied on the two τ candidates at the last trigger level are 29 GeV on the leading τ candidate and 20 GeV on the subleading one. With respect to the event selection described in Section 4, the total signal efficiency of the di-$\tau_{\mathrm{h}ad}$ trigger is $\approx 60\%$.

Events that pass the trigger are selected as collision events if they have a reconstructed vertex that is formed by three or more tracks and lies within 15 cm of the nominal interaction point along the beam axis.

The cross sections for Higgs boson production in the gluon fusion process have been calculated using HIGLU [15] and ggh@nnlo [16]. For the b-quark associated production, a matching scheme described in Ref. [17] is used to combine the NLO calculation for $gg \to b\bar{b}A/H/h$ in the 4-flavor scheme [18, 19] and the NNLO calculation for $b\bar{b} \to A/H/h$ in the 5-flavor scheme [20]. In both cases, the MSTW2008 set of parton distribution functions (PDFs) [21] has been used.

The masses, couplings, and branching ratios of the Higgs bosons are computed with FeynHiggs [22]. Details of the calculations and associated strong coupling constant α_S, PDFs and scale uncertainties can be found in [23]. The direct $gg \to A/H/h$ production is simulated with POWHEG [24], and the associated $b\bar{b}A/H/h$ production with SHERPA [25]. Both $gg \to A$ and $b\bar{b}A$ samples are generated at values of m_A in the range from 90 to 600 GeV. To obtain simulated samples for the decays of the H and h bosons, events with A boson decays with mass m_A closest to m_H and m_h respectively are scaled to the H/h production cross section. For any given m_A and $\tan\beta$, the masses m_H and m_h of the H and h bosons are calculated in the m_h^{max} MSSM benchmark scenario [26] and A boson events with m_A closest to m_H and m_h, respectively, are combined with these samples with appropriately scaled cross sections to obtain a signal sample for $A/H/h$ production. The increase of the Higgs boson natural width with $\tan\beta$ is neglected as it is small compared with the experimental resolution of the mass definition used. Table 1 shows the signal cross section times branching ratio for $\tan\beta = 20$ at $m_A = 120$, 200 and 300 GeV.

The production of W or Z bosons that subsequently decay into leptons constitutes the most important background for the $e\mu$ and $\ell\tau_{had}$ final states. These processes include W+jets, Z/γ^*, where γ^* denotes a virtual photon, top-quark ($t\bar{t}$ and single-top) and electroweak di-boson (WW, WZ, ZZ) production. Here, $Z/\gamma^* \to \tau^+\tau^-$ events constitute an irreducible background for Higgs boson masses close to the Z boson mass. $Z/\gamma^* \to \ell^+\ell^-$ ($\ell = e, \mu$) events contribute if one of the charged leptons or an accompanying jet is misidentified. QCD jet processes provide a significant background contribution if there are real leptons from decays of heavy quarks or if jets are misidentified as electrons, muons, or τ_{had} decays. In contrast to the other final states, QCD jet processes are the dominant background in the $\tau_{had}\tau_{had}$ final state as it is more probable for a jet to be misidentified as a hadronic τ decay than as a light lepton.

The production of W and Z bosons in association with jets is simulated with the ALPGEN [27] and PYTHIA [28] generators. The $t\bar{t}$ and single-top processes are generated with MC@NLO ($t\bar{t}$ and single-top s-channel) and ACER MC [29](single-top t- and Wt-channels) and, for di-boson production, HERWIG [30] and MC@NLO are used. The loop-induced process $gg \to WW$ is generated with gg2WW [31]. For events generated with ALPGEN, HERWIG, MC@NLO, and gg2WW, parton shower and hadronization are simulated with HERWIG and the underlying event with JIMMY [32]. The programs TAUOLA [33, 34] and PHOTOS [35] are used to model the decays of τ leptons and the QED radiation in decays, respectively, in all event samples except those generated with SHERPA which includes these processes internally.

Table 1 summarizes the inclusive cross sections for the above processes, which are used to normalize the simulated event samples. The cross section for single gauge boson production is calculated at NNLO in QCD perturbation theory [36], for $t\bar{t}$ production at NLO+NLL [37,38], and for single-top and di-boson

Table 1: Cross sections for signal and background processes. For $A/H/h$ production, the cross section is multiplied by the branching ratio for $A/H/h \to \tau^+\tau^-$. The signal cross sections are given for $\tan\beta = 20$ and the three values quoted correspond to $A/H/h$ production, respectively. For $m_A = 120/200/300$ GeV and $\tan\beta = 20$, the H and h boson masses in the m_h^{max} scenario are $m_H = 132/200/300$ GeV and $m_h = 118/130/130$ GeV.

Signal process	$\sigma \times$ BR [pb]
$b\bar{b}A/H/h(\to \tau\tau)$, $m_A = 120$ GeV	7.62/0.69/7.3
$gg \to A/H/h(\to \tau\tau)$, $m_A = 120$ GeV	4.93/2.21/4.1
$b\bar{b}A/H/h(\to \tau\tau)$, $m_A = 200$ GeV	0.49/0.49/0.02
$gg \to A/H/h(\to \tau\tau)$, $m_A = 200$ GeV	0.13/0.16/0.46
$b\bar{b}A/H/h(\to \tau\tau)$, $m_A = 300$ GeV	0.02/0.03/0.002
$gg \to A/H/h(\to \tau\tau)$, $m_A = 300$ GeV	0.003/0.005/0.11
Background process	**σ [pb]**
$W \to \ell$ ($\ell = e, \mu, \tau$)	10.5×10^3
$Z/\gamma^* \to \ell^+\ell^-$ ($m_{\ell\ell} > 10$ GeV)	4.96×10^3
$t\bar{t}$	165
Single-top (t-, s- and Wt-channels)	58.7, 3.9, 13.1
Di-boson (WW, WZ and ZZ)	46.2, 18.0, 5.6

production at NLO [39]. For the background processes the PDFs MSTW2008 ($W \to \ell$, $Z/\gamma^* \to \ell^+\ell^-$, single-top and di-boson) and CTEQ6.6 [40] ($t\bar{t}$) are used.

No simulated samples for the QCD jet background are analysed, as this background is entirely estimated from data.

All simulated samples are processed through a full simulation of the ATLAS detector based on GEANT4 [41, 42]. To match the pile-up (overlap of several proton-proton collisons) observed in the data, minimum-bias events [43, 44] are overlaid to the generated signal and background events, and the resulting events are reweighted so that the average number of interactions per bunch crossing agrees with the data. Two types of pile-up effects were considered in the simulated events: in-time pile-up effects, which are due to the overlap of several interactions in the same bunch crossing, and out-of-time pile-up effects, which are due to the overlap of interactions in consecutive bunch crossings.

3 Object reconstruction

Electron candidates are reconstructed from a cluster in the electromagnetic calorimeter that is matched to a track in the inner detector. The cluster must have a profile consistent with an electromagnetic shower [45]. Electron candidates are required to have a transverse momentum above 15 GeV and a pseudorapidity $|\eta| < 1.37$ or $1.52 < |\eta| < 2.47$. Muon candidates are reconstructed by combining tracks in the muon spectrometer with tracks in the inner detector [45]. They must have a transverse momentum above 10 GeV and a pseudorapidity in the range $|\eta| < 2.5$. Isolation requirements are imposed on electron and muon candidates by requiring that the additional transverse energy in the calorimeter cells in a cone of radius $\Delta R = \sqrt{(\Delta\eta)^2 + (\Delta\phi)^2} = 0.2$ centered on the electron or muon direction is less than 8% of the electron transverse energy, and less than 4% of the muon transverse momentum. In addition, the sum of the transverse momenta of all tracks with $p_T > 1$ GeV in a cone of radius $\Delta R = 0.4$ around the lepton direction must be less than 6% of the lepton track transverse momentum.

The reconstruction of candidates for hadronic τ decays is based on calorimeter jets reconstructed with the anti-k_T algorithm [46,47] with a distance parameter $\Delta R = 0.4$, seeded using three-dimensional topological calorimeter energy clusters. Their identification, including vetoing electrons and muons, is based on observables that describe the shape of the calorimeter shower and on tracking information, which are combined in a boosted decision tree (BDT) discriminator for the $\ell\tau_{had}$ and a likelihood discriminator for the $\tau_{had}\tau_{had}$ channel [48]. A τ_{had} candidate must have a visible transverse momentum, $p_{T\tau_{had}}$, above 20 GeV, a pseudorapidity in the range $|\eta| < 2.5$, 1 or 3 associated tracks of $p_T > 1$ GeV, and a total charge of ± 1, computed from all tracks associated with the candidate. The efficiency of the likelihood (BDT) τ identification for τ candidates with $p_{T,\tau_{had}} > 20$ GeV is about 55% (60%) and the probability to misidentify a jet as a τ lepton, as determined from a di-jet control sample, is about 5% (5%). When candidates fulfilling the above criteria overlap with each other geometrically (within $\Delta R < 0.2$), only one of them is selected. The overlap is resolved by selecting muons, electrons and τ_{had} candidates in this order of priority.

The missing transverse momentum in the event, $E_{\mathrm{T}}^{\mathrm{miss}} = \sqrt{(E_{\mathrm{x}}^{\mathrm{miss}})^2 + (E_{\mathrm{y}}^{\mathrm{miss}})^2}$, is reconstructed as the vector sum of all topological calorimeter energy clusters in the region $|\eta| < 4.5$ and corrected for identified muons [45].

4 Event selection

The signatures of $A/H/h \to \tau^+\tau^- \to e\mu 4\nu$ signal events are one isolated electron, one isolated muon and $E_{\mathrm{T}}^{\mathrm{miss}}$ due to the undetected neutrinos from the two τ decays, where either one of the leptons can trigger the event. If the event was triggered by the electron trigger a reconstructed electron with $p_{\mathrm{T}}^{e} > 22$ GeV and a muon with $p_{\mathrm{T}}^{\mu} > 10$ GeV and opposite electric charge is required. Otherwise, if the event was triggered by the muon trigger only it is required that there is a reconstructed muon with $p_{\mathrm{T}}^{\mu} > 20$ GeV and a reconstructed electron with $p_{\mathrm{T}}^{e} > 15$ GeV and opposite electric charge.

In order to suppress backgrounds from $t\bar{t}$, single-top and di-boson production two additional requirements are applied: the scalar sum of the transverse momentum of the electron, the transverse momentum of the muon and the missing transverse momentum must be smaller than 120 GeV, and the azimuthal opening angle between the electron and the muon must be larger than 2.0 rad.

The signatures of $A/H/h \to \tau^+\tau^- \to e/\mu\tau_{\mathrm{had}} 3\nu$ signal events, where one τ lepton decays leptonically and the other hadronically, are an isolated electron or muon, ℓ, a τ_{had} candidate, and $E_{\mathrm{T}}^{\mathrm{miss}}$ due to the undetected neutrinos from the two τ decays. Exactly one electron or muon with $p_{\mathrm{T}}^{e} > 25$ GeV or $p_{\mathrm{T}}^{\mu} > 20$ GeV and one oppositely-charged τ_{had} candidate with $p_{T,\tau_{had}} > 20$ GeV are required in the event. Events with more than one electron or muon reconstructed, using less strict requirements on the leptons, are rejected to suppress events from $Z/\gamma^* \to \ell^+\ell^-$ ($\ell = e, \mu$) decays and from $t\bar{t}$ or single-top production. For electrons, the transverse momentum threshold is lowered to $p_{\mathrm{T}}^{e} > 15$ GeV and less strict identification criteria are applied. Muons are used with a lowered transverse momentum threshold of $p_{\mathrm{T}}^{\mu} > 10$ GeV and without requiring them to be isolated. Events with jets from QCD processes as well as $Z/\gamma^* \to \ell^+\ell^-$ ($\ell = e, \mu$) decays are rejected by requiring $E_{\mathrm{T}}^{\mathrm{miss}} > 20$ GeV. Events with real leptons from $W \to \ell\nu$ decays are suppressed by requiring the transverse mass of the ℓ-$E_{\mathrm{T}}^{\mathrm{miss}}$ system, defined as

$$m_{\mathrm{T}} = \sqrt{2 p_{\mathrm{T}}^{\ell} E_{\mathrm{T}}^{\mathrm{miss}} (1 - \cos\Delta\phi)}, \tag{1}$$

to be below 30 GeV. Here, p_{T}^{ℓ} is the transverse momentum of the electron or muon and $\Delta\phi$ is the angle between the electron or muon and the $E_{\mathrm{T}}^{\mathrm{miss}}$ vector in the plane perpendicular to the beam direction.

The $A/H/h \to \tau^+\tau^- \to \tau_{had}\tau_{had}\nu\nu$ signature is characterized by two identified hadronic tau decays and missing transverse momentum from the undetected neutrinos. Events with exactly two oppositely charged τ_{had} candidates that match the τ_{had} trigger objects inside a cone of radius $\Delta R = 0.2$ around the direction of the τ_{had} candidates are selected. The highest-p_T τ_{had} candidate is required to have

Table 2: Number of selected events in data and expected events from Monte Carlo (MC) simulation for a data sample corresponding to 1.06 fb^{-1}. The total $A/H/h$ signal yields for m_A = 120 GeV and $\tan\beta$ = 20 for the $e\mu$ and $\ell\tau_{had}$ final states and m_A = 200 GeV and $\tan\beta$ = 20 for the $\tau_{had}\tau_{had}$ final state are shown in the rightmost column. No MC expectation is given for the QCD jet background because this background can only be reliably estimated with data (it amounts to 120 ± 20, 202 ± 25 and 157 ± 18 events for the $e\mu$, the combined $e\tau_{had}$ and $\mu\tau_{had}$ and the $\tau_{had}\tau_{had}$ final states, respectively, as described in Sections 6.2, 6.3 and 6.4). For the $e\tau_{had}$ and $\mu\tau_{had}$ final state the quoted estimate of the W+jets background does not take the normalization from the control region as described in Section 6.3 into account. The estimate for $Z/\gamma^* \to \tau^+\tau^-$ is using the embedding technique as described in Section 6.1 for the $e\mu$, $e\tau_{had}$ and $\mu\tau_{had}$ final states. Only the statistical component of the uncertainties is shown.

	Data	Total MC bkg (w/o QCD)	W+jets	Di-boson	$t\bar{t}$+ single-top	$Z/\gamma^* \to$ $ee,\mu\mu$	$Z/\gamma^* \to$ $\tau^+\tau^-$	A/H/h signal
$e\mu$	2472	2496±27	30±15	109±5	100±2	40±4	2217±22	155±6
$e\tau_{had}$	626	775±40	188±31	4.1±0.5	33± 3	64±5	486±24	41±4
$\mu\tau_{had}$	1287	1378±43	239±33	5.4±0.6	51±4	105±7	978±26	75±5
$\tau_{had}\tau_{had}$	245	76± 7	25±5	1.4±0.3	2.0±0.9	-	48±5	19±1

$p_{T,\tau_{had}} > 45$ GeV and the second-highest-p_T candidate to have $p_{T,\tau_{had}} > 30$ GeV to ensure that both τ_{had} candidates are on the plateau of the trigger efficiency and to suppress backgrounds from Z, W boson production and QCD multijet production. To further reject QCD jet processes and Z boson production a missing transverse momentum of $E_{\mathrm{T}}^{\mathrm{miss}} > 25$ GeV is required. Finally, events are rejected if they contain an electron candidate with $p_{\mathrm{T}}^{e} > 15$ GeV or a muon candidate with $p_{\mathrm{T}}^{\mu} > 10$ GeV, isolation is not required.

Corrections are applied to simulation to account for differences in the τ_{had} trigger efficiency between data and simulation. These are derived as a function of $p_{T,\tau_{had}}$ of the reconstructed τ_{had} candidate and the associated trigger, using $Z \to \tau_\mu\tau_{had}$ control regions from data and simulation [49], where τ_μ denotes a τ reconstructed in the $\mu 2\nu$ final state. Trigger and misidentification scale factors for jets misidentified as τ_{had} decays were measured from data using associated jets from $W \to \mu\nu$ events and are applied to Monte Carlo. The event selection criteria to isolate $W \to \mu\nu$ decays are based on Ref. [50]. These criteria have been shown to achieve a purity large than 90% and a QCD contamination of less than 1%.

Table 2 compares the number of selected events in data with those expected from the simulation of various background processes, not including QCD jet production. After the full selection, 2472, 626, 1287, and 245 data events are observed in the $e\mu$, $e\tau_{had}$, $\mu\tau_{had}$, and $\tau_{had}\tau_{had}$ channels, respectively. The estimation of backgrounds based on data control samples used for the final results of the analysis is discussed in Section 6. The signal efficiency for m_A = 120 GeV (m_A = 200 GeV) amounts to 9 (11)% in the $e\mu$, 3 (8)% in the $\ell\tau_{had}$ and 0.1 (1.3)% in the $\tau_{had}\tau_{had}$ final state.

5 Di-Tau mass reconstruction

After the selection of signal candidates, different $\tau^+\tau^-$ mass reconstruction methods are studied. The simplest one is the so-called visible $\tau^+\tau^-$ mass, $m_{\tau\tau}^{\mathrm{visible}}$, defined as the invariant mass of visible tau decay products. It can be expanded to the effective mass, $m_{\tau\tau}^{\mathrm{effective}}$ by calculating the invariant mass of the visible tau decay products and the $E_{\mathrm{T}}^{\mathrm{miss}}$ system according to

$$m_{\tau\tau}^{\mathrm{effective}} = \sqrt{(p_{\tau^+} + p_{\tau^-} + p_{\mathrm{miss}})^2}, \tag{2}$$

where p_{τ^+} and p_{τ^-} denote the four-vectors of the electron, the muon or τ_{had} candidates, respectively, and the missing momentum four-vector is defined as $p_{\text{miss}} = (E_{\text{T}}^{\text{miss}}, E_{\text{x}}^{\text{miss}}, E_{\text{y}}^{\text{miss}}, 0)$.

An accurate mass reconstruction of a di-tau system is challenging due to the presence of multiple neutrinos resulting in an $E_{\text{T}}^{\text{miss}}$ signature. A technique introduced in Ref. [51] is applied for the first time in ATLAS. In the following, this method is referred to as the Missing Mass Calculator (MMC) and is described for the $\ell\tau_{had}$ final state.

Conceptually, the MMC is a more sophisticated version of the well-known collinear approximation [52]. The major difference is that the MMC does not assume a strict collinearity of the visible and invisible τ decay products (i.e., $\phi_{\text{neutrino(s)}}=\phi_{\text{visible }\tau}$ and $\theta_{\text{neutrino(s)}}=\theta_{\text{visible }\tau}$). For each di-$\tau$ event, the MMC solves a system of four equations:

$$E_x^{\text{miss}} = p_{\text{miss}_1} \sin\theta_{\text{miss}_1} \cos\phi_{\text{miss}_1} + p_{\text{miss}_2} \sin\theta_{\text{miss}_2} \cos\phi_{\text{miss}_2}, \tag{3}$$

$$E_y^{\text{miss}} = p_{\text{miss}_1} \sin\theta_{\text{miss}_1} \sin\phi_{\text{miss}_1} + p_{\text{miss}_2} \sin\theta_{\text{miss}_2} \sin\phi_{\text{miss}_2}, \tag{4}$$

$$\begin{aligned} m_\tau^2 &= m_{\text{miss}_1}^2 + m_{\text{vis}_1}^2 + 2\sqrt{p_{\text{vis}_1}^2 + m_{\text{vis}_1}^2}\sqrt{p_{\text{miss}_1}^2 + m_{\text{miss}_1}^2}, \\ &\quad -2 p_{\text{vis}_1} p_{\text{miss}_1} \cos\Delta\theta_{\text{vm}_1}, \end{aligned} \tag{5}$$

$$\begin{aligned} m_\tau^2 &= m_{\text{vis}_2}^2 + 2\sqrt{p_{\text{vis}_2}^2 + m_{\text{vis}_2}^2} \cdot p_{\text{miss}_2}, \\ &\quad -2 p_{\text{vis}_2} p_{\text{miss}_2} \cos\Delta\theta_{\text{vm}_2} \end{aligned} \tag{6}$$

where E_x^{miss} and E_y^{miss} are the x- and y-components of the $E_{\text{T}}^{\text{miss}}$ vector, p_{vis_1}, m_{vis_1}, θ_{vis_1}, ϕ_{vis_1} are the momentum, the invariant mass, the polar and the azimuthal angle of the leptonic τ decay products, p_{vis_2}, m_{vis_2}, θ_{vis_2}, ϕ_{vis_2} are the momentum, the invariant mass, the polar and the azimuthal angle of the hadronic τ decay products, and m_τ=1.777 GeV is the τ lepton invariant mass. The other quantities are unknown, namely the combined momenta $p_{\text{miss}_{1,2}}$ of the neutrino (or neutrinos) for each of the two decaying τ leptons and the invariant mass of the neutrinos in the leptonic τ decay, m_{miss_1}. Finally, $\Delta\theta_{\text{vm}_{1,2}}$ is the angle between the vectors p_{miss} and p_{vis} for each of the two τ leptons, and it can be expressed in terms of the other variables. The number of unknowns exceeds the number of constraints and thus the system is solved for a grid of points in the ($\Delta\phi_1$, $\Delta\phi_2$) parameter space, where $\Delta\phi_i$ is the difference between the azimuthal angles of the visible and invisible tau decay products. To determine the best estimate for the di-τ invariant mass in a given event, the $m_{\tau\tau}$ distribution from all scanned points in the grid are produced. At each scanned point the 3-dimensional angle between the momentum vector of the visible τ decay products and the neutrino momentum vector $\Delta\theta_{3D}$ is calculated and the obtained di-τ mass is weighted by a corresponding probability density function. Figure 1 shows examples of the angular probabilities for three types of τ decays. These probability densities are obtained from a sample of simulated $Z \to \tau^+\tau^-$ events. As a cross-check, similar probability functions are obtained from a signal sample of H(120)$\to \ell\tau_{\text{had}}$ events, and it is found that the angular distances are identical within the uncertainties. The position of the maximum of the obtained $m_{\tau\tau}$ distribution is used as the final estimator $m_{\tau\tau}^{\text{MMC}}$ for a given event. For leptonic decays, the dimensionality of the parameter space is increased to account for the unknown value of m_{miss} of the two neutrinos in each of the leptonically decaying τ leptons in the event. The effects of finite $E_{\text{T}}^{\text{miss}}$ resolution are taken into account by introducing two additional scans for the possible values of E_x^{miss} and E_y^{miss}, according to the measured $E_{\text{T}}^{\text{miss}}$ resolution, given by $\sigma(E_{\text{T}}^{\text{miss}})=\text{A}_0\sqrt{\Sigma E_T}$ with $\text{A}_0=0.50\pm0.05$ [53].

As shown in Table 3 for the $\ell\tau_{had}$ final state, the MMC has a high efficiency[1] above 96% for signal samples with mass m_H<250 GeV and for Z background processes. The efficiency for non-Z backgrounds is smaller; it varies from 87% (W) to 93% (QCD), depending on the process. The MMC mass resolution

---

[1] The MMC efficiency is the ratio of the number of events for which MMC finds a solution, over the number of events which is given as an input to the algorithm.

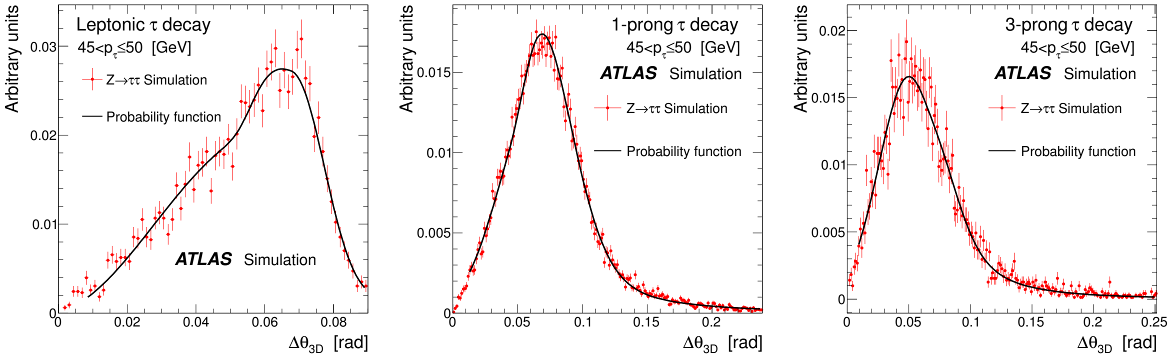

Figure 1: Angular distance distributions between neutrinos and visible decay products for τ leptons with generated momentum $45 < p \leq 50$ GeV obtained from simulated $Z \to \tau\tau$ events. The three distributions correspond to the three dominant types of τ decays. The solid black line shows the functions used in the calculations of global event probabilities. These distributions ideally depend only on the decay type and the initial momentum of the τ lepton.

Table 3: MMC efficiency for the $\ell\tau_{had}$ final state for the Z boson background and for signal samples of mass m_H=120 GeV, m_H=150 GeV, m_H=200 GeV, m_H=250 GeV, m_H=300 GeV and m_H=400 GeV.

	Z	H(120)	H(150)	H(200)	H(250)	H(300)	H(400)
Efficiency (%)	98	99	98	98	96	91	88

for Z background and for signal masses up to 150 GeV is about 17%. For the higher signal masses considered, the MMC resolution is below ≈ 23%.

In the analyses described in this note, the effective mass, $m_{\tau\tau}^{\text{effective}}$, is used for the $e\mu$ final state, the MMC mass, $m_{\tau\tau}^{\text{MMC}}$, for the $\ell\tau_{\text{had}}$ final state and the visible mass, $m_{\tau\tau}^{\text{visible}}$, for the $\tau_{\text{had}}\tau_{\text{had}}$ final state.

6 Background estimation

In the search for a Higgs boson signal the normalization and shape of the final mass distributions for the sum of all background contributions have to be determined. Data control samples are used, where possible, to estimate or validate the most relevant background sources: $Z/\gamma^* \to \tau^+\tau^-$ and QCD multi-jet production in the $e\mu$ final state, W+jets, $Z/\gamma^* \to \tau^+\tau^-$, and QCD multi-jet production in the $\ell\tau_{had}$ final state and QCD jet production in the $\tau_{had}\tau_{had}$ final state. The remaining backgrounds given in Table 2 are estimated from simulation.

6.1 Estimation of the electroweak background shapes

The shapes of the mass distributions for the irreducible $Z/\gamma^* \to \tau^+\tau^-$ background can be determined from data with a so-called embedding technique. This technique starts from a data sample of $Z/\gamma^* \to \mu^+\mu^-$ events with an invariant mass of $m_{\mu\mu} > 40$ GeV, in which the muons are replaced by simulated τ leptons. To avoid a possible bias on the embedded objects, the two muons with a transverse momentum above 20 GeV are selected without any isolation requirement, while effects from additional background contamination are estimated within the systematic variations described in Section 7. The muon tracks and calorimeter cells in a cone of radius $\Delta R < 0.1$ around the direction of the muon are removed from the event. Then an event fragment containing only two τ leptons that have the same kinematics as the muons

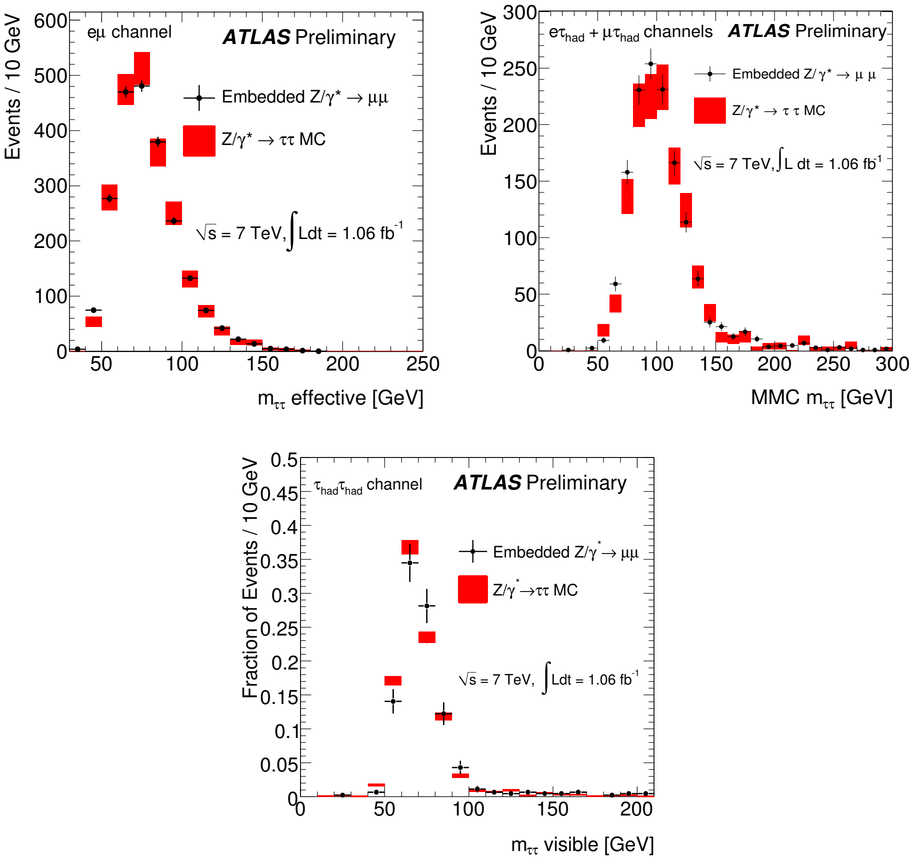

Figure 2: Effective mass distribution for the $e\mu$ final state (top left), MMC mass distribution for the $\ell\tau_{had}$ (top right) and visible mass distribution for the $\tau_{had}\tau_{had}$ (bottom) final states for simulated $Z/\gamma^* \to \tau^+\tau^-$ events (boxes) and τ-embedded $Z/\gamma^* \to \mu^+\mu^-$ events (points) passing the signal selection. The size of the boxes and the length of the error bars indicate the statistical uncertainty on the simulated and τ-embedded samples, respectively.

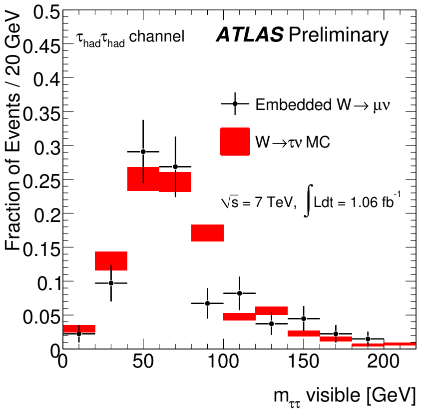

Figure 3: Visible mass distribution for the $\tau_{had}\tau_{had}$ final state for simulated $W \to \tau\nu$ events (boxes) and τ-embedded $W \to \mu\nu$ events (points) passing the signal selection. The size of the boxes and the length of the error bars indicate the statistical uncertainty on the simulated and τ-embedded samples, respectively.

and whose decays are generated by TAUOLA [33] is passed through the ATLAS detector simulation. The original data event, from which the muons have been removed, and the simulated event fragment are combined and a full reconstruction of the resulting new event is performed. Thus, only the τ decays and the corresponding detector response are taken from simulation while the underlying Z boson kinematics and all other properties of the event are obtained from the $Z/\gamma^* \rightarrow \mu^+\mu^-$ data.

Figure 2 compares the mass distributions of the τ-embedded sample with simulated $Z/\gamma^* \rightarrow \tau^+\tau^-$ events for the $e\mu$, $\ell\tau_{had}$, and $\tau_{had}\tau_{had}$ final states.

A good agreement within the statistical uncertainties is observed, validating the use of the method to estimate the $Z/\gamma^* \rightarrow \tau^+\tau^-$ background from embedded $Z/\gamma^* \rightarrow \mu^+\mu^-$ data, in which all pile-up effects are assumed to be described better than in the simulation. For the $e\mu$ and $\ell\tau_{had}$ final states the embedding samples are normalized to the yields predicted by simulation after selecting an $e\mu$ or $\ell\tau_{had}$ pair with opposite charge and then used for the rest of the selection. The $\tau_{had}\tau_{had}$ final state uses the embedding samples to verify the shapes predicted by simulation as the size of the embedding sample is limited compared to the simulated sample.

For the $\tau_{had}\tau_{had}$ final state, the W+jets background is validated with an embedding technique as well. A sample of $W \rightarrow \mu\nu$ decays is selected based on Ref. [50] and the muon is replaced by a simulated hadronic τ decay. Also here, a good agreement between the τ-embedded sample and the $W \rightarrow \tau\nu$ simulation is observed, as shown in Figure 3.

6.2 Background from QCD processes in the $e\mu$ final state

For the estimation of the background from QCD processes, four independent samples are selected by using selection criteria on two variables: the isolation of the electron and muon and their charge product. The signal region A is defined by the selection criteria given above, i.e. opposite-sign isolated leptons. The other regions are background control regions mostly populated by events from QCD processes. Region B contains same-sign isolated leptons, region C opposite-sign anti-isolated leptons, and region D same-sign anti-isolated leptons. Anti-isolated leptons are obtained by inverting the isolation criteria described in Section 3. The shape of the $m_{\tau\tau}^{\text{effective}}$ distribution in the signal region A is taken from control region C and the normalization is derived by $n_A = r_{C/D} \times n_B$. Here, n_A and n_B denote the event yields in regions A and B and $r_{C/D}$ the ratio of the event yields in regions C and D after subtracting the contribution from non-QCD backgrounds estimated from simulation. This method relies on the assumption that the two variables used to define the four regions are uncorrelated and that the shape of the $m_{\tau\tau}^{\text{effective}}$ distribution does not depend on the isolation or charge product requirement. This has been verified by comparing the event yields and shapes of the $m_{\tau\tau}^{\text{effective}}$ distribution in data for regions C and D and in further control regions defined by the requirement of one isolated and one anti-isolated lepton.

After subtracting the contribution from non-QCD backgrounds, estimated from simulation, the jet event yield in regions B, C and D are found to be $n_B = 60 \pm 10(stat.)$, $n_C = (1.01 \pm 0.01(stat.)) \times 10^4$ and $n_D = (5.07 \pm 0.07(stat.)) \times 10^3$. The ratio $r_{C/D}$ is determined to be $r_{C/D} = 2.00 \pm 0.03(stat.)$. The jet event yield in the signal region is therefore estimated to be $n_A^{QCD} = 120 \pm 20(stat.)$. The resulting $m_{\tau\tau}^{\text{effective}}$ distribution is shown in Fig. 4. Systematic uncertainties are discussed in Section 7.

6.3 Background estimation for the $\ell\tau_{had}$ final state

Two methods that mainly focus on estimating the QCD and W+jets backgrounds [54] are discussed. They are based on data, simulation and the samples obtained from the embedding procedure described in Section 6.1. It is assumed that the shape of the MMC mass distribution is the same for opposite-sign (OS) and same-sign (SS) background events apart from the $Z/\gamma^* \rightarrow \tau^+\tau^-$ background.

The QCD and W+jets background estimate from the first method is used for the limit extraction in Section 8. The assumptions that the shape of the MMC distribution for these backgrounds is the same for opposite-sign and same-sign events and that their ratio is the same in the signal region, defined by the nominal selection, and in background-enhanced QCD and W+jets control regions have been verified with simulated events. The OS backgrounds are therefore estimated from data as same-sign events and the difference between OS and SS is added from simulation. For the remaining backgrounds the differences between opposite-sign and same-sign events is estimated from simulation and added to the same-sign data sample to get the full background estimate.

The total number of opposite-sign background events in the signal region, n_{OS}^{Bkg}, can be expressed as

$$n_{\mathrm{OS}}^{Bkg} = n_{\mathrm{SS}}^{Bkg} + n_{\mathrm{OS-SS}}^{W} + n_{\mathrm{OS-SS}}^{Z} + n_{\mathrm{OS-SS}}^{\mathrm{other}}, \tag{7}$$

where n_{SS}^{Bkg} is the sum of all same-sign backgrounds in the signal region and the remaining terms are the differences between opposite-sign and same-sign events for the W+jets, $Z/\gamma^* \to \tau^+\tau^-$, and other backgrounds. The ratio of opposite-sign and same-sign events for the QCD background, $r_{OS/SS}^{\mathrm{QCD}}$, is expected to be close to unity and therefore $n_{\mathrm{OS-SS}}^{\mathrm{QCD}} = 0$ is assumed. The assumption $r_{OS/SS}^{\mathrm{QCD}} \approx 1$ is checked with a data control sample that is dominated by low-E_{T} jets from QCD processes, as expected in the signal region. This sample is selected by replacing the requirement $E_{\mathrm{T}}^{\mathrm{miss}} > 20$ GeV with $E_{\mathrm{T}}^{\mathrm{miss}} < 15$ GeV and relaxing the isolation of the electron or muon candidate. After subtraction of the other backgrounds using simulation, a value of $r_{OS/SS}^{\mathrm{QCD}} = 1.12 \pm 0.01(stat.) \pm 0.09(syst.)$ is obtained. The observed deviation of $r_{OS/SS}^{\mathrm{QCD}}$ from unity is taken into account in the determination of systematic uncertainties for the final result.

For the W+jets background, a significant deviation of the ratio $r_{\mathrm{OS/SS}}^{W}$ from unity is expected since W+jets production is dominated by gu/gd-processes that often give rise to a jet originating from a quark whose charge is anti-correlated with the W boson charge.

Each of the terms in Eq. 7 is estimated separately and for each bin in the MMC mass distribution, thus not only an estimation of the background normalization but also of the MMC mass shape is obtained. The total number of same-sign events n_{SS}^{Bkg} is determined for the nominal selection except for changing the opposite-sign charge requirement to same-sign. In the full MMC mass range, $314 \pm 32(stat.)$ same-sign events are selected in data. The contributions from $Z/\gamma^* \to \tau^+\tau^-$, taken from the samples described in Section 6.1 is $n_{\mathrm{OS-SS}}^{Z} = (1.45 \pm 0.04(stat.)) \times 10^3$ and from other backgrounds, taken from simulation is $n_{\mathrm{OS-SS}}^{\mathrm{other}} = 209 \pm 11(stat.)$. The W+jets term in Eq. 7 is estimated to be $n_{\mathrm{OS}}^{W} = 126 \pm 13(stat.)$, where the ratio $r_{\mathrm{OS/SS}}^{W} = 2.6 \pm 0.1(stat.)$ is taken into account. This ratio is obtained in a W+jets-dominated data control region selected by replacing the $m_{\mathrm{T}} < 30$ GeV requirement in the nominal selection by $m_{\mathrm{T}} > 50$ GeV. A small remaining contribution from backgrounds other than W+jets is subtracted based on simulation and the $Z/\gamma^* \to \tau^+\tau^-$ samples described in Section 6.1. It has been checked in simulation that this ratio is approximately independent of the m_{T} range and can thus be used for the signal region. The value of n_{OS}^{W} is obtained by scaling the number of events in the W+jets control region by the ratio of events in the signal and control regions determined from simulation. The shape of the MMC mass distribution for this contribution is taken from simulation.

The total background estimate obtained from Eq. 7 is $n_{\mathrm{OS}}^{Bkg} = (2.10 \pm 0.05(stat.)) \times 10^3$, which can be compared to 1913 events observed in data. The resulting MMC mass distribution is shown in Fig. 4.

The second method provides separate estimates of the QCD and W+jets background contributions and is used to cross-check the results of the method described above. For the QCD jet background the same method and assumptions as described in Section 6.2 for the $e\mu$ final state are used, but replacing one of the leptons (e or μ) by the τ_{had} candidate and using the MMC distribution instead of $m_{\tau\tau}^{\mathrm{effective}}$. The shape of the MMC distribution is taken from region B and scaled by the ratio of event yields in regions C and D: $r_{C/D} = 1.14 \pm 0.03(stat.)$. The resulting estimate of the QCD jet background in the signal region is $n_{A}^{\mathrm{QCD}} = r_{C/D} \times n_B = 202 \pm 25(stat.)$. The estimate of the W+jets background is obtained by deriving normalization scale factors of $0.6 \pm 0.1(stat.)$ for the opposite-sign and 0.8 ± 0.1 for the same-sign

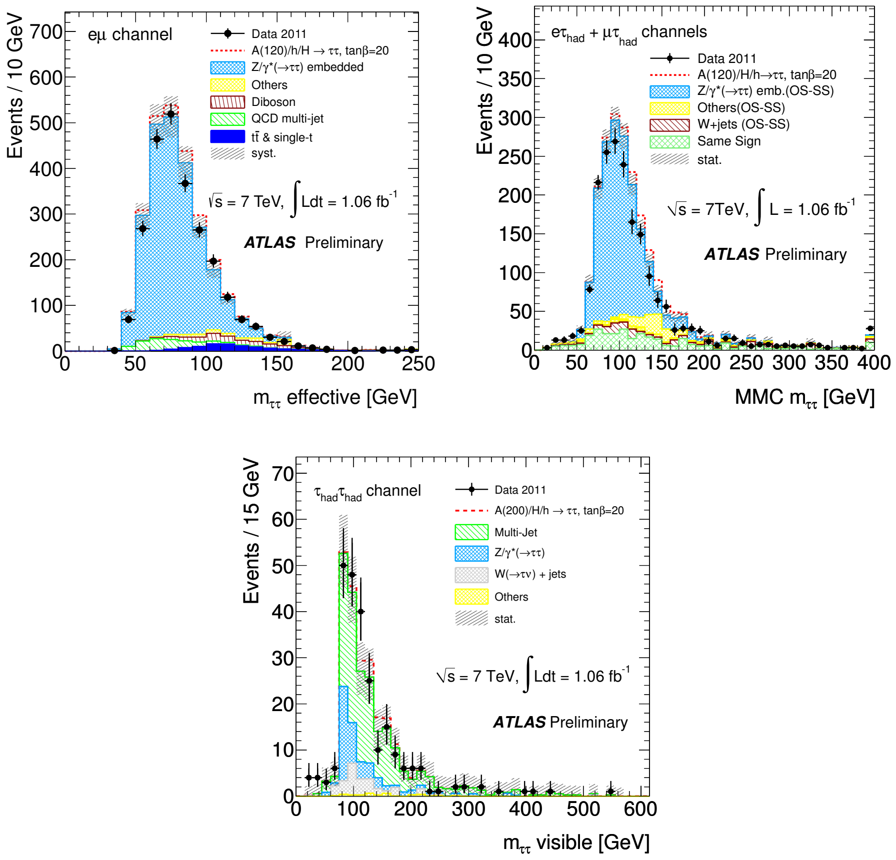

Figure 4: Effective mass distribution for the $e\mu$ (top left), MMC mass distribution for the $\ell\tau_{had}$ (top right) and visible mass distribution for the $\tau_{had}\tau_{had}$ (bottom) final states. The data are compared with the background expectation and an added hypothetical MSSM signal (m_A = 120GeV, $tan\beta$ = 20 for top plots, m_A = 200GeV, $tan\beta$ = 20 for the bottom plot). "OS-SS" denotes the difference between the opposite-sign and same-sign event yields.

region for the normalization of the simulated MMC distribution in a W-dominated data control sample. This control region is defined by replacing the $m_{\mathrm{T}} < 30$ GeV requirement in the nominal selection by $70 < m_{\mathrm{T}} < 120$ GeV. The MMC mass shape of the W+jets background is taken from simulation. The estimated number of W+jets events for the nominal selection amounts to $250 \pm 23(\textit{stat.})$ events. Adding the expected number of events for $Z/\gamma^* \to \tau^+\tau^-$ and the other backgrounds from simulation to the sum of the estimated yields from QCD and W+jets processes, a total background contribution of $(2.16 \pm 0.05(\textit{stat.})) \times 10^3$ events is obtained, which agrees well with the first background estimation method. The shapes of the MMC mass distributions determined by both methods are also found to agree.

6.4 Background estimation for the $\tau_{had}\tau_{had}$ final state

The QCD jet background is estimated by using a similar method as described in Sections 6.2 and 6.3. Here, the four control regions are defined by selection criteria on the charge product of the two τ candidates and the tightness of the τ identification criteria. For the latter, the nominal τ identification used in this analysis has been relaxed to obtain so-called *loose* τ candidates, corresponding to an 80% tau identification efficiency. The signal region A is defined by the nominal selection criteria of the $\tau_{had}\tau_{had}$ channel. Region B contains same-sign τ candidates using the nominal τ identification, region C opposite-sign *loose* τ candidates, and region D same-sign *loose* τ candidates. In the regions with *loose* τ candidates, those candidates that also pass the nominal identification have been rejected to obtain independent control samples.

The shape of the $m_{\tau\tau}^{\mathrm{visible}}$ distribution is taken from region C and scaled by the ratio of event yields in regions B and D, obtained after subtraction of the non-QCD background contributions. The shape of the $m_{\tau\tau}^{\mathrm{visible}}$ distribution is taken from region C as it has a sufficiently large number of events to reduce the influence of the dominating statistical uncertainty.

The resulting estimate for the QCD jet background in the signal region is $n_A^{\mathrm{QCD}} = r_{B/D} \times n_C = 157 \pm 18(\textit{stat.})$ events. This estimate has been cross-checked with an estimation that is based on the same method, but uses selection criteria on the missing transverse momentum ($E_{\mathrm{T}}^{\mathrm{miss}} < 20$ GeV and $E_{\mathrm{T}}^{\mathrm{miss}} > 25$ GeV) instead of the charge product to define the control regions. This results in an estimated QCD jet background of $n_A^{\mathrm{QCD}} = 155 \pm 8(\textit{stat.})$ events, in good agreement with the previous result.

The electroweak backgrounds $Z/\gamma^* \to \tau^+\tau^-$ and $W \to \tau\nu$ are the other two sizable background components in the $\tau_{had}\tau_{had}$ final state. They are estimated from simulation and validated with data using samples of $Z \to \mu\mu$ and $W \to \mu\nu$ decays, as described in Section 6.1.

6.5 Validation of the background models

The level of agreement between the data and background models can be judged from Figures 5, 6 and 7 for the three final states. Added is a hypothetical signal for MSSM Higgs bosons.

Figure 5 shows the distribution of the scalar sum of the transverse momentum of the electron, the transverse momentum of the muon and the missing transverse momentum, and the azimuthal opening angle between the electron and the muon for the $e\mu$ final state.

To illustrate the performance of the estimates in the $\ell\tau_{had}$ final state, Figure 6 shows the p_{T} spectrum of the τ_{had} candidate and $E_{\mathrm{T}}^{\mathrm{miss}}$ obtained with the first method and the MMC mass distribution obtained with the second method.

Finally for the $\tau_{had}\tau_{had}$ final state, Figure 7 shows the distribution of $E_{\mathrm{T}}^{\mathrm{miss}}$, the p_{T} spectrum of the two τ_{had} candidates and the $\Delta\phi(\tau_{had}^1\tau_{had}^2)$ for data and the background estimates.

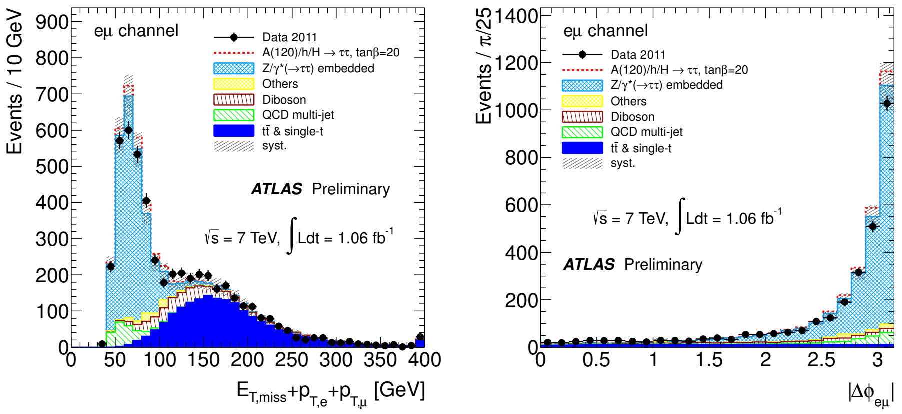

Figure 5: Distribution of kinematic variables for the $e\mu$ final state. The scalar sum of the transverse momentum of the electron, the transverse momentum of the muon and the missing transverse momentum is shown on the left after preselection. On the right is the azimuthal opening angle between the electron and the muon after selecting events having the scalar sum to be less than 120 GeV.

7 Systematic uncertainties

Systematic effects on the signal efficiency and the estimated number of background events can be grouped in four categories: theoretical inclusive cross sections, acceptance, knowledge of detector performance and systematic uncertainties of the data-driven approaches to estimate the background contributions.

The uncertainty on the theoretical inclusive cross section for each individual signal and background process is obtained from variations of the renormalization and factorization scales (μ_R, μ_F) by factors $1/2$ and 2 and a variation of the strong coupling constant and the PDF sets within their uncertainties. The uncertainty on the acceptance is estimated by varying μ_R, μ_F, the matching parameters in ALPGEN and the choice of the PDF to MRST2001J [55] in the generation of simulated event samples.

The uncertainty on the trigger efficiencies for electrons and muons is 1%. For the τ_{had} triggers the efficiency uncertainty is determined from data in $p_{T,\tau_{had}}$ intervals for hadronic τ decays and jets that are misidentified as hadronic τ decays. The uncertainty for jets that are misidentified as hadronic τ decays is combined with the uncertainty of the offline misidentification probability, resulting in a combined uncertainty of $\approx$ 10%. The uncertainties due to the limited knowledge of the detector performance are evaluated by varying the trigger, reconstruction and identification efficiencies for electrons, muons and τ candidates, and by varying the energy resolution and energy scale of electrons, muons, τ candidates, and energy deposits outside of these objects. These are propagated in a fully correlated way into the $E_{\mathrm{T}}^{\mathrm{miss}}$ scale and resolution. The size of the uncertainties from the different sources on the various background processes which are partially or completely estimated from simulated events are summarized in Table 4. The luminosity uncertainty is 3.7% [14].

The difference in the impact of the energy scale and resolution uncertainty on the expected event yields in the $\ell\tau_{had}$ and $e\mu$ final states is caused by requiring a hadronic τ decay with $p_{T,\tau_{had}} > 20$ GeV and a lower threshold $E_{\mathrm{T}}^{\mathrm{miss}} > 20$ GeV in the $\ell\tau_{had}$ final states, whereas in the $e\mu$ final state only an upper threshold of $p_{\mathrm{T}}^{e} + p_{\mathrm{T}}^{\mu} + E_{\mathrm{T}}^{\mathrm{miss}} < 120$ GeV is required. For the $\tau_{had}\tau_{had}$ channel, it is caused by requiring the two hadronic τ decays with $p_{T,\tau_{had}} > 30$ GeV and $p_{\mathrm{T}}^{\tau,vis} > 45$ GeV and a lower threshold $E_{\mathrm{T}}^{\mathrm{miss}} > 25$ GeV. The uncertainties, apart from the ones related to the data-driven techniques, are treated as fully correlated between the three final states.

The systematic uncertainty from the data-driven estimate of the QCD background in the $e\mu$ final state corresponds to 23 events. It includes the systematic uncertainty on the subtracted non-QCD background (2.4 events) and on the assumption of identical $m_{\tau\tau}^{\mathrm{effective}}$ shapes in the different control regions which

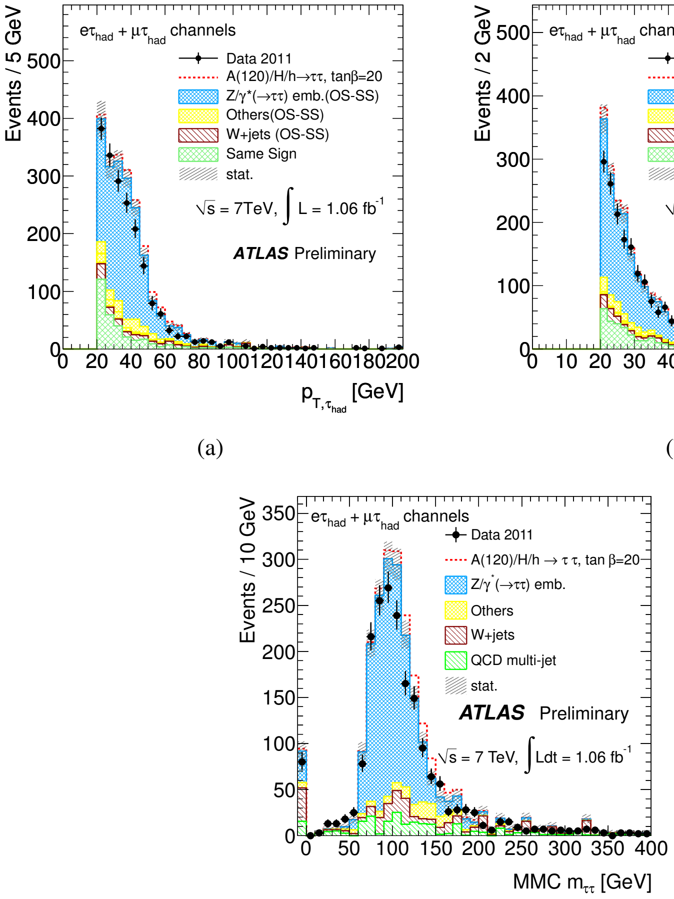

(a)

(b)

(c)

Figure 6: Distribution of kinematic variables for the $\ell\tau_{had}$ final state after full event selection. Figures (a) and (b) are obtained with the first background estimation method as described in Section 6.3 and show the transverse momentum of the τ_{had} candidate and the missing transverse momentum. Figure (c) is obtained with the second background estimation method (see Section 6.3) and shows the MMC mass distribution. To illustrate the MMC efficiency, events where the fit is not converging are shown in the bin below zero.

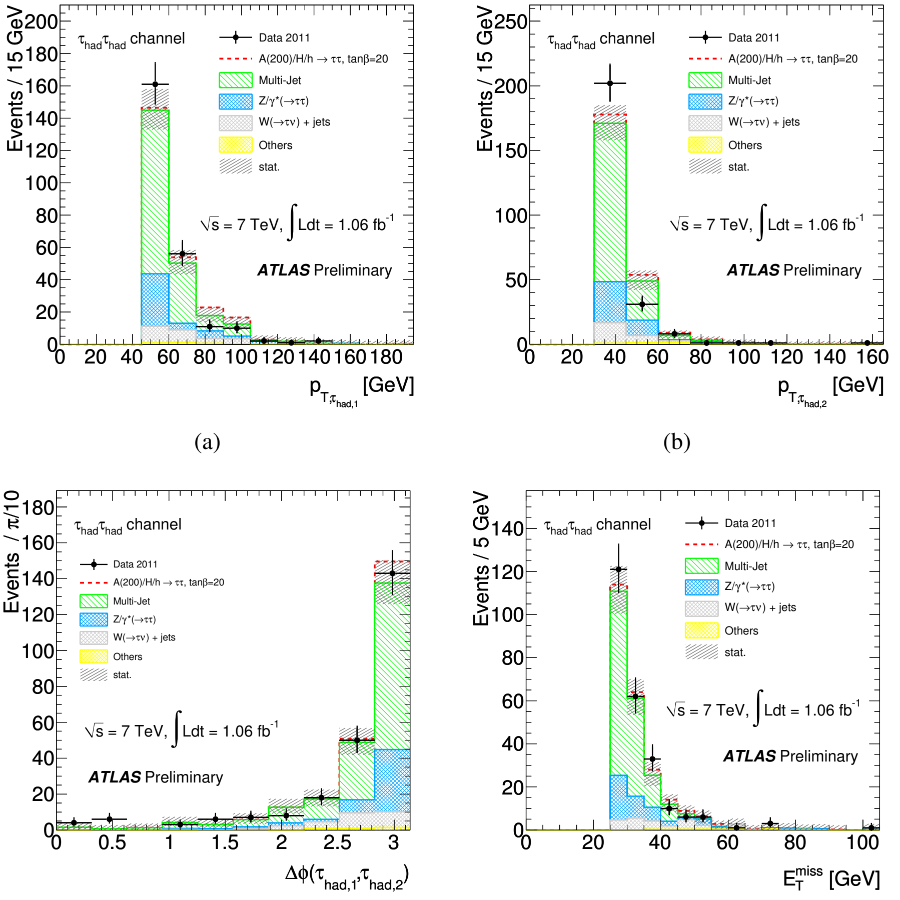

(a) (b)

(c) (d)

Figure 7: Distribution of kinematic variables for the $\tau_{had}\tau_{had}$ final state after full event selection. (a) distribution of the p_{T} spectrum of the τ_{had} candidate with highest transverse momentum (b), distribution of the p_{T} spectrum of the τ_{had} candidate with second highest transverse momentum, (c) distribution of $\Delta\phi(\tau^1_{had}\tau^2_{had})$ and (d) distribution of the missing transverse momentum.

Table 4: Uncertainties on the number of selected events for those background contributions that are at least partially estimated from simulation and for a hypothetical signal (m_A = 120 GeV and $\tan\beta = 20$ for the $e\mu$ and $\ell\tau_{had}$ final states and m_A = 200 GeV and $\tan\beta = 20$ for the $\tau_{had}\tau_{had}$ final state). All numbers are given in %. When three numbers are given the first refers to the $e\mu$ final state, the second to the $\ell\tau_{had}$ final states and the third to the $\tau_{had}\tau_{had}$ final state. If an uncertainty does not apply for a certain background, this is indicated by a "-". For the $e\mu$ final state, the uncertainty on the W+jets background is dominated by the statistical component and the systematic uncertainty is neglected; for the $\ell\tau_{\mathrm{had}}$ final state the W+jets background is estimated from data.

	W+jets	Di-boson	$t\bar{t}$+ single-top	$Z/\gamma^* \to$ $ee, \mu\mu$	$Z/\gamma^* \to$ $\tau^+\tau^-$	Signal
$\sigma_{inclusive}$	-/-/5	7	10	5/5/-	5	14/14/16
Acceptance	-/-/20	4/2/7	3/2/9	2/14/-	5/14/14	5/7/9
e efficiency	-/-/0.8	4/3.1/0.5	4/3.6/0.3	4/3.1/-	4/3.0/0.5	4/3.6/0.1
μ efficiency	-/-/0.3	2/1.2/0.4	2/1.1/0.0	2/1.3/-	2/1.8/0.4	2/1.0/0.1
τ efficiency and fake rate	-/-/21	-/9.1/15	-/9.1/13	-/48/-	-/9.1/15	-/9.1/15
Energy scales and resolution	-/-/$^{+34}_{-21}$	2/$^{+19}_{-9}$/$^{+26}_{-12}$	6/$^{+5}_{-4}$/12	1/$^{+39}_{-25}$/-	1/11/$^{+63}_{-23}$	1/$^{+30}_{-23}$/$^{+9}_{-8}$
Luminosity	-/-/3.7	3.7	3.7	3.7/3.7/-	3.7	3.7
Total uncertainty	-/-/$^{+45}_{-36}$	10/$^{+23}_{-16}$/$^{+32}_{-22}$	13/15/23	8/$^{+64}_{-56}$/-	9/21/$^{+67}_{-31}$	16/$^{+35}_{-30}$/$^{+26}_{-25}$

results in an uncertainty on $r_{C/D}$ of 0.39. The final estimate for the jet yield in the signal region is $n_A^{QCD} = 120 \pm 20(stat.) \pm 23(syst.) = 120 \pm 30$.

For the $\ell\tau_{had}$ channels, the most important uncertainties for the data-driven estimation of the QCD jet and W+jets backgrounds (see Eq. 7) are the statistical uncertainty on the number of same-sign events in the signal region (17%) and the uncertainty on the ratios $r^{\mathrm{QCD}}_{OS/SS}$ (19%) and $r^{W}_{\mathrm{OS/SS}}$ (11%). An additional uncertainty of 10% is derived from the m_{T} dependence of $r^{W}_{\mathrm{OS/SS}}$ i.e., for the extrapolation from the control to the signal region. The final estimate for the total background yield is $n^{Bkg}_{\mathrm{OS}} = (2.1 \pm 0.1(stat.) \pm 0.3(syst.)) \times 10^3 = (2.1 \pm 0.3) \times 10^3$. For the second background estimation method in addition to the uncertainties described above the correction factors applied for the W+jets normalization are varied within their uncertainty and propagated to the QCD estimate. The estimate for the QCD background is $n_{QCD} = 217 \pm 25(stat.) \pm 48(syst.)$, W+jets background $n_W = 250 \pm 22(stat.) \pm 22(syst.)$ and for the total background is $n_{total} = (2.2 \pm 0.1(stat.) \pm 0.3(syst.)) \times 10^3 = (2.2 \pm 0.3) \times 10^3$.

For the $\tau_{had}\tau_{had}$ channel, the statistical uncertainty on the number of same-sign events in the signal region (8.7%) is the dominant uncertainty of the data-driven estimate of the QCD jet contribution. The systematic uncertainties on the non-QCD background contributions in the control regions are propagated to the QCD estimate. The systematic uncertainty of $\approx 3\%$ is dominated by the energy scale and jet $\to \tau$ misidentification efficiency uncertainty. The QCD estimate is $n_{QCD} = 157 \pm 18(stat.) \pm 4(syst.) = 157 \pm 18$, the estimate for the total background yield is $n^{Bkg}_{\mathrm{OS}} = 233 \pm 19(stat.)^{+35}_{-19}(syst.) = 233^{+40}_{-27}$.

For the energy scale uncertainty, variations of the electron, muon, τ_{had} candidate, and $E_{\mathrm{T}}^{\mathrm{miss}}$ not only changes in normalization but also in the shapes of the discriminating mass variables are observed and therefore included as an additional uncertainty in the derivation of the Higgs boson exclusion limits in Section 8. In the channels where embedded data are used, systematic uncertainties are derived for the final decay products that are taken from simulation.

Systematic effects of the embedding method are estimated from variations of the embedding procedure. While for the default method no isolation is required for the selected muons in order to avoid a bias on the embedded objects, the procedure is repeated on $Z/\gamma^* \to \mu^+\mu^-$ data fulfilling standard isolation criteria for the $e\mu$ and the $\ell\tau_{had}$ channel. A second variation accounts for the energy deposition from the selected muons in the calorimeter, which is by default completely removed in a cone of radius $\Delta R < 0.1$ around the muon direction. The systematic uncertainties from these variations enter the limit calculation in the form of shape systematics. All other systematic uncertainties have no significant effect on the mass shape. Combining the estimated contribution from the various background processes and their uncertainties results in the final background estimate shown in Table 5.

Table 5: Observed numbers of events in data, for an integrated luminosity of 1.06 fb^{-1}, and total expected background contributions for the final states considered in this analysis, with their combined statistical and systematic uncertainties.

Final state	Exp. Background	Data
$e\mu$	$(2.6 \pm 0.2) \times 10^3$	2472
$\ell\tau_{had}$	$(2.1 \pm 0.4) \times 10^3$	1913
$\tau_{had}\tau_{had}$	$233\,^{+44}_{-28}$	245
Sum	$(4.9 \pm 0.6) \times 10^3$	4630

8 Results

No significant excess of events compared with the Standard Model expectation is observed in the data in any of the final states. Exclusion limits at the 95% confidence level are set on the production cross section times branching ratio, $\sigma \times \mathrm{BR}(\phi \to \tau\tau)$, of a generic Higgs boson ϕ as a function of its mass, m_ϕ, and for MSSM Higgs boson $A/H/h$ production as a function of the parameters m_A and $\tan\beta$. The exclusion limits are derived with the profile likelihood method [56] based on the CL_s parameter [57,58] from an analysis of the $m_{\tau\tau}^{\mathrm{effective}}$ distribution for the $e\mu$ final state, the $m_{\tau\tau}^{\mathrm{MMC}}$ distribution for the $\ell\tau_{had}$ final state and the $m_{\tau\tau}^{\mathrm{visible}}$ distribution for the $\tau_{had}\tau_{had}$ final state.

Systematic uncertainties are separated into common, fully correlated (energy scale, acceptance, luminosity) and channel-specific ones for the limit derivation, and are included as nuisance parameters. The $m_{\tau\tau}^{\mathrm{effective}}$, $m_{\tau\tau}^{\mathrm{MMC}}$ and $m_{\tau\tau}^{\mathrm{visible}}$ shape uncertainties due to the uncertainties on the energy scales of leptons, hadronic τ candidates and $E_{\mathrm{T}}^{\mathrm{miss}}$ for the backgrounds obtained from simulation are taken into account. Asymptotic formulae are used to find the median expected limit along with the $\pm 1\sigma$ and $\pm 2\sigma$ error bands. Figure 8 shows the resulting cross section limits for the final states and their combination. The cross section limit is evaluated for signal acceptances of two different production processes, $gg \to \phi$ and b-quark associated production which can differ from the SM Higgs boson by the coupling strength. The $\ell\tau_{had}$ final states provide the most stringent limit over a large part of the accessible Higgs boson mass range. The $e\mu$ and $\tau_{had}\tau_{had}$ final states lead to improvements of the exclusion limits for small and large Higgs boson masses, respectively. The limits on the production of neutral MSSM Higgs bosons $A/H/h$ in the $\tan\beta - m_A$ plane, for the m_h^{max} scenario and Higgsino mass parameter $\mu > 0$, are shown in Fig. 9. The combined limit and the influence of the individual channels to the combination is shown in Figure 10.

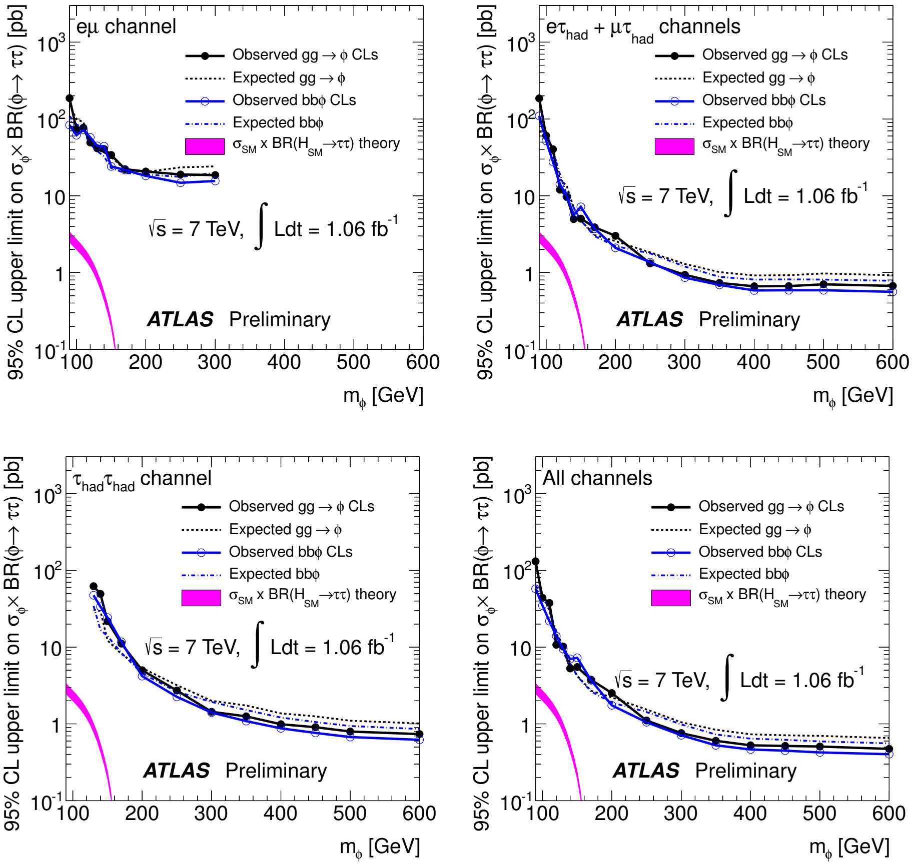

Figure 8: Expected and observed limits on the production cross section and branching ratio for a generic Higgs boson ϕ, $\sigma_\phi \times BR(\phi \rightarrow \tau^+\tau^-)$, at the 95% confidence level, as a function of the Higgs boson mass for both production modes considered. The solid and dashed lines show the observed and expected exclusion limits, respectively. For comparison the SM cross section, $\sigma_{SM} \times BR(H_{SM} \rightarrow \tau^+\tau^-)$, is also shown. The limits are shown for the $e\mu$ (top left), $\ell\tau_{had}$ (top right), $\tau_{had}\tau_{had}$ (bottom left) final states and for their combination (bottom right).

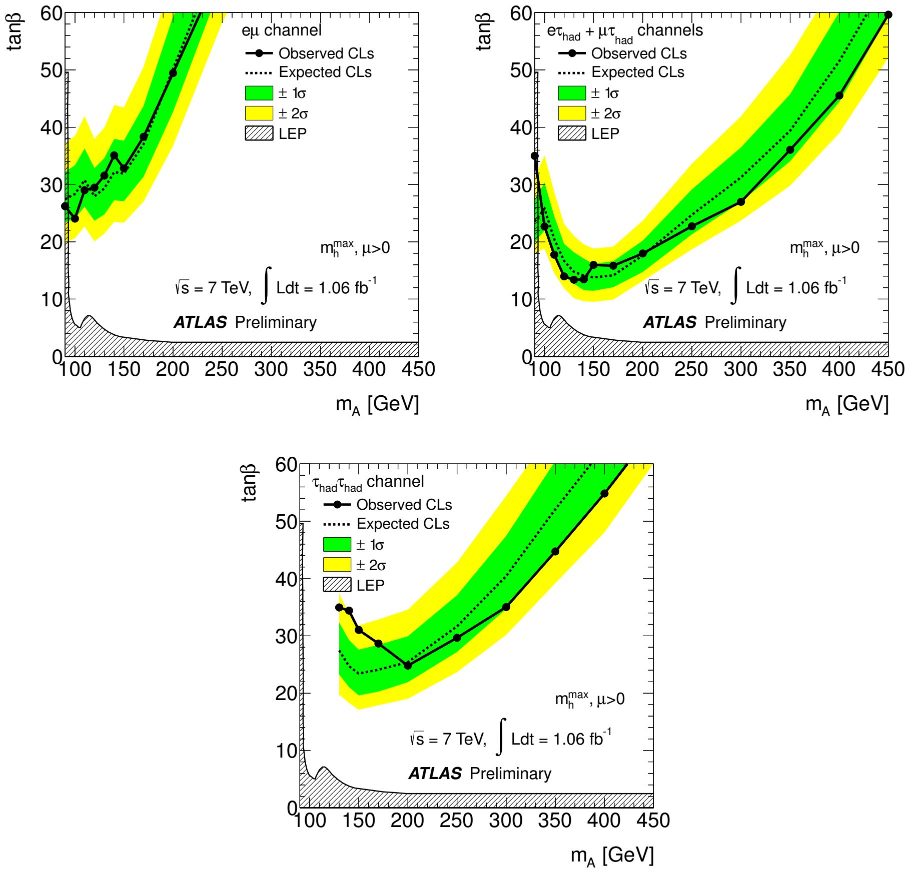

Figure 9: Expected and observed exclusion limits based on CL_s in the $m_A - \tan\beta$ plane of the MSSM. The limits are shown for the $e\mu$ (upper left), $\ell\tau_{had}$ (upper right),$\tau_{had}\tau_{had}$ (lower center) final states. The region above the drawn limit curve is excluded at the 95% confidence level. The dark grey (green) and light grey (yellow) bands correspond to the $\pm1\sigma$ and $\pm2\sigma$ error bands, respectively.

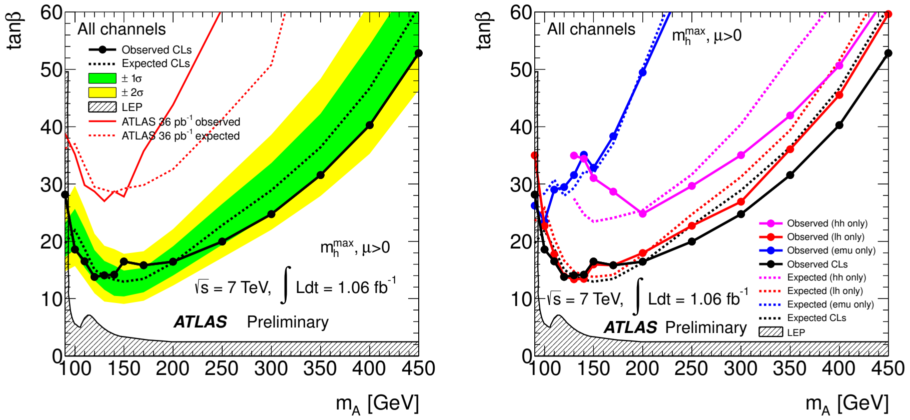

Figure 10: Expected and observed exclusion limits based on CL_s in the $m_A - \tan\beta$ plane of the MSSM derived from the combination of the analyses for the $e\mu$, $\ell\tau_{had}$ and $\tau_{had}\tau_{had}$ final states. The exclusion limits from a previous result and from LEP are also shown (left). The contribution of the individual channels to the combined limit is shown (right). The region above the drawn limit curve is excluded at the 95% confidence level. The dark grey (green) and light grey (yellow) bands correspond to the $\pm1\sigma$ and $\pm2\sigma$ error bands, respectively.

9 Conclusions

In this note, a search for neutral MSSM Higgs bosons $A/H/h$ with the ATLAS detector in proton-proton collisions corresponding to an integrated luminosity of 1.06 fb^{-1} at a center-of-mass energy of 7 TeV is presented. Candidates for $A/H/h \rightarrow \tau^+\tau^-$ decays are selected in the four final states $e\mu$, $e\tau_{had}$, $\mu\tau_{had}$ and $\tau_{had}\tau_{had}$. No evidence for a Higgs boson signal is observed in the reconstructed mass spectra. Exclusion limits on both the cross section for the production of a generic Higgs boson ϕ as a function of its mass and on MSSM Higgs boson production $A/H/h$ as a function of m_A and $\tan\beta$, are derived. These results exclude regions of parameters space beyond the existing limits from previous experiments at LEP [59] and the Tevatron [10, 11] and are similar to those recently obtained by the CMS Collaboration [12].

10 Acknowledgements

We thank CERN for the very successful operation of the LHC, as well as the support staff from our institutions without whom ATLAS could not be operated efficiently.

We acknowledge the support of ANPCyT, Argentina; YerPhI, Armenia; ARC, Australia; BMWF, Austria; ANAS, Azerbaijan; SSTC, Belarus; CNPq and FAPESP, Brazil; NSERC, NRC and CFI, Canada; CERN; CONICYT, Chile; CAS, MOST and NSFC, China; COLCIENCIAS, Colombia; MSMT CR, MPO CR and VSC CR, Czech Republic; DNRF, DNSRC and Lundbeck Foundation, Denmark; ARTEMIS, European Union; IN2P3-CNRS, CEA-DSM/IRFU, France; GNAS, Georgia; BMBF, DFG, HGF, MPG and AvH Foundation, Germany; GSRT, Greece; ISF, MINERVA, GIF, DIP and Benoziyo Center, Israel; INFN, Italy; MEXT and JSPS, Japan; CNRST, Morocco; FOM and NWO, Netherlands; RCN, Norway; MNiSW, Poland; GRICES and FCT, Portugal; MERYS (MECTS), Romania; MES of Russia and ROSATOM, Russian Federation; JINR; MSTD, Serbia; MSSR, Slovakia; ARRS and MVZT, Slovenia; DST/NRF, South Africa; MICINN, Spain; SRC and Wallenberg Foundation, Sweden; SER, SNSF and Cantons of Bern and Geneva, Switzerland; NSC, Taiwan; TAEK, Turkey; STFC, the Royal Society and Leverhulme Trust, United Kingdom; DOE and NSF, United States of America.

The crucial computing support from all WLCG partners is acknowledged gratefully, in particular from CERN and the ATLAS Tier-1 facilities at TRIUMF (Canada), NDGF (Denmark, Norway, Sweden), CC-IN2P3 (France), KIT/GridKA (Germany), INFN-CNAF (Italy), NL-T1 (Netherlands), PIC (Spain), ASGC (Taiwan), RAL (UK) and BNL (USA) and in the Tier-2 facilities worldwide.

References

[1] L. Evans and P. Bryant, JINST 3 (2008) S08001.

[2] F. Englert and R. Brout, Phys. Rev. Lett. 13 (1964) 321.

[3] P. W. Higgs, Phys. Lett. 12 (1964) 132.

[4] P. W. Higgs, Phys. Rev. Lett. 13 (1964) 508.

[5] P. W. Higgs, Phys. Rev. 145 (1966) 1156.

[6] G. S. Guralnik, C.R. Hagen and T. W. B. Kibble, Phys. Rev. Lett. 13 (1964) 585.

[7] H. P. Nilles, Phys. Rep. 110 (1984) 1.

[8] H. E. Haber and G. L. Kane, Phys. Rep. 117 (1985) 75.

[9] The ATLAS Collaboration, JINST 3 (2008) S08003.

[10] The CDF and D0 Collaborations and Tevatron New Physics Higgs Working Group (TEVNPHWG), arXiv:1003.3363 [hep-ex].

[11] The D0 Collaboration, V.M. Abazov et al., arXiv:1106.4885 [hep-ex].

[12] The CMS Collaboration, S. Chatrchyan et al., arXiv:CMS PAS HIG-11-009.

[13] The ATLAS Collaboration arXiv:1107.5003 [hep-ex].

[14] The ATLAS Collaboration, ATLAS-CONF-2011-130.

[15] M. Spira, hep-ph/9510347.

[16] R. Harlander and W. B. Kilgore, Phys. Rev. Lett. 88 (2002) 201801.

[17] R. Harlander, M. Krämer and M. Schumacher,
CERN-PH-TH/2011-134 - FR-PHENO-2011-009 - TTK-11-17 - WUB/11-04,
https://twiki.cern.ch/twiki/pub/LHCPhysics/MSSMNeutral/santandermatching-hks.pdf.

[18] S. Dittmaier, M. Kramer and M. Spira, Phys. Rev. D70 (2004) 074010.

[19] S. Dawson, C. B. Jackson, L. Reina and D. Wackeroth, Mod. Phys. Lett. A21 (2006) 89.

[20] R. Harlander and W. B. Kilgore, Phys. Rev. D68 (2003) 013001.

[21] A. D. Martin, W. J. Stirling, R. S. Thorne, and G. Watt, Eur. Phys. J. C63 (2009) 189–285.

[22] M. Frank et al., JHEP 0702 (2007) 047.

[23] The LHC Higgs Cross Section Working Group, S. Dittmaier, C. Mariotti, G. Passarino, R. Tanaka (Eds.) et al., arXiv:1101.0593 [hep-ph].

[24] S. Alioli, et al., Higgs boson production in gluon fusion, JHEP 02 (2009) 029.

[25] T. Gleisberg et al., JHEP 02 (2009) 007.

[26] M. Carena, S. Heinemeyer, C. E. M. Wagner, and G. Weiglein, Eur. Phys. J. C26 (2003) 601.

[27] M. L. Mangano et al., JHEP 07 (2003) 001.

[28] T. Sjöstrand, S. Mrenna and P. Skands, JHEP 05 (2006) 026.

[29] B. Kersevan, E.Richter-WasarXiv:hep-ph/0405247.

[30] G. Corcella et al., JHEP 01 (2001) 010.

[31] T. Binoth, M. Ciccolini, N. Kauer and M. Kramer, JHEP 12 (2006) 046.

[32] J. M. Butterworth, J. R. Forshaw and M. H. Seymour, Z. Phys. C72 (1996) 637.

[33] S. Jadach, Z. Was, R. Decker and J. H. Kuhn, Comput. Phys. Commun. 76 (1993) 361.

[34] P. Golonka, B. Kersevan, T. Pierzchala, E. Richter-Was, Z. Was and M. Worek, Comput. Phys. Commun. 174 (2006) 818.

[35] E. Barberio and Z. Was, Comput. Phys. Commun. 79 (1994) 291.

[36] R. Gavin, Y. Li, F. Petriello and S. Quackenbush, arXiv:1011.3540 [hep-ph].

[37] S. Moch and P. Uwer, Nucl. Phys. Proc. Suppl. 183 (2008) 75.

[38] U. Langenfeld, S. Moch and P. Uwer, arXiv:0907.2527 [hep-ph].

[39] S. Frixione and B. R. Webber, JHEP 06 (2002) 029.

[40] P.M. Nadolsky et al., Phys. Rev. D 78 (2008) 013004.

[41] The GEANT4 Collaboration, S. Agostinelli et al., Nucl. Instrum. Meth. A506 (2003) 250.

[42] The ATLAS Collaboration, Eur. Phys. J. C70 (2010) 823.

[43] The ATLAS Collaboration, ATL-PHYS-PUB-2010-014.

[44] The ATLAS Collaboration, ATLAS-CONF-2010-031.

[45] The ATLAS Collaboration, JHEP 12 (2010) 060.

[46] M. Cacciari, G. P. Salam and G. Soyez, JHEP 04 (2008) 063.

[47] M. Cacciari and G. P. Salam, Phys. Lett. B 641 (2006) 57.

[48] The ATLAS Collaboration, ATLAS-CONF-2011-077.

[49] The ATLAS Collaboration, ATLAS-CONF-2011-010.

[50] The ATLAS Collaboration, ATLAS-CONF-2011-041.

[51] A. Elagin, P. Murat, A. Pranko, A. Safonov, Accepted by NIMA – http://dx.doi.org/10.1016/j.nima.2011.07.009. arXiv:1012.4686.

[52] The ATLAS Collaboration, CERN-OPEN-2008-020, arXiv:0901.0512.

[53] The ATLAS Collaboration, ATLAS-CONF-2011-080.

[54] The ATLAS Collaboration, ATLAS-CONF-2010-096.

[55] A.D. Martin, R.G. Roberts, W.J. Stirling, R.S. Thorne, arXiv:0110215v2.

[56] G. Cowan, K. Cranmer, E. Gross and O. Vitells, Eur. Phys. J. C71 (2011) 1554.

[57] T. Junk, Nucl. Instrum. Meth. A434 (1999) 435.

[58] A. L. Read, J. Phys. G28 (2002) 2693.

[59] ALEPH Collaboration, DELPHI Collaboration, L3 Collaboration, OPAL Collaboration and LEP Working Group for Higgs Boson Searches, Eur. Phys. J. C47 (2006) 547–587.

11 Appendix: Standard Model limit

In addition to the MSSM limit, a Standard Model limit was derived as well, in the $\ell\tau_{had}$ final state. It is shown in Fig. 11. POWHEG gluon-fusion and vector boson-fusion signal samples in a mass range from 100 to 150GeV are used.

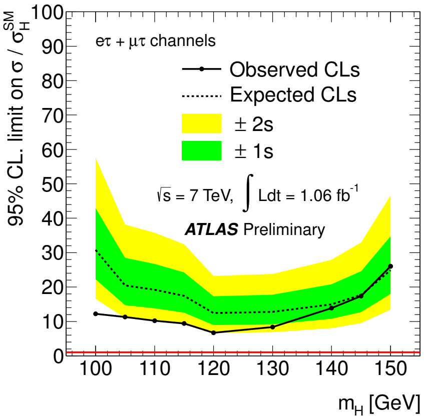

Figure 11: Expected and observed limits, at the 95% confidence level, on the production of a Standard Model Higgs boson in the $\ell\tau_{had}$ final state. The solid and dashed lines show the observed and expected exclusion limits, respectively.